Research Square

Preprints are preliminary reports that have not undergone peer review.
They should not be considered conclusive, used to inform clinical practice,
or referenced by the media as validated information.

# Optimization of Mixing Performance for a Twin-Shaft Paddle Feed Mixer Based on Discrete Element Method

**Wei Song**
Jinggangshan University
**Bin Luo**
Jinggangshan University
**Yongkun Zhang**
Jinggangshan University
**Hongyun Liu**
1670702479@qq.com

Guizhou Industry Polytechnic University

**Article**

**Keywords:** Twin-shaft paddle mixer, Total mixed ration, Discrete element method, Mixing uniformity, Response surface methodology, Finite-element analysis

**Posted Date:** November 26th, 2026

**DOI:** https://doi.org/10.21203/rs.3.rs-11596898/v1

**License:** This work is licensed under a Creative Commons Attribution 4.0 International License.
Read Full License

**Additional Declarations:** No competing interests reported.

# Optimization of Mixing Performance for a Twin-Shaft Paddle Feed Mixer Based on Discrete Element Method

Wei Song[a], Bin Luo[a], Yongkun Zhang[a], Liu Hongyun[b*]

[a]*Jiangxi Provincial Key Laboratory of Modern Agricultural Equipment, School of Mechanical Engineering, Jinggangshan University, Ji'an 343009, China*

[b]*Guizhou Industry Polytechnic University, Guiyang 551400, China*

** Corresponding author: Liu Hongyun. E-mail address: 1670702479@qq.com*

## Abstract

To address the uneven dispersion of trace components, material retention, and limited mixing efficiency of conventional horizontal single-shaft paddle mixers, a twin-shaft paddle-type total mixed ration (TMR) mixer was designed. Axial convection was adopted as the primary mixing mechanism and radial shear as a secondary mechanism. The paddle installation angle, rotor spacing, and main-shaft rotational speed were identified as the principal design and operating variables. A discrete-element model combined with response-surface methodology was used to quantify their effects on the Lacey mixing index, M. The simulations revealed a closed circulation pattern characterized by axial transport along the paddle flights and central cross-shaft recirculation. The influence of the factors on mixing uniformity decreased in the order of main-shaft rotational speed, paddle installation angle, and rotor spacing. Constrained optimization yielded 60 r/min, 45°, and 400 mm, respectively; the simulated Lacey index at this configuration was 0.91. A linear elastic finite-element screening further indicated that the rotor shaft remained below the tabulated yield strength under a 1.30 shock factor, while the lowest flexible modes remained well above the rated rotational frequency. These simulation results provide a preliminary design basis for improving the mixing uniformity and structural reliability of twin-shaft paddle mixers.

***Keywords***: *Twin-shaft paddle mixer; Total mixed ration; Discrete element method; Mixing uniformity; Response surface*

*methodology; Finite-element analysis*

## 0. Introduction

Mixing is a critical unit operation in compound feed production because it directly affects nutrient uniformity, animal growth performance, feed conversion efficiency, and production economics (Bergeron et al., 2026; Lyu et al., 2020; Wanapat et al., 2024). A total mixed ration (TMR) is a nutritionally balanced mixture of roughage, concentrate, and additives prepared according to the requirements of ruminants at different growth stages. The trend toward large-scale, precision feed production has increased the demand for mixers that combine high uniformity, short cycle times, and reliable operation (Niu et al., 2022; Schären et al., 2016; Sova et al., 2014; Tian et al., 2020).

Horizontal twin-shaft paddle mixers are widely used in small- and medium-sized feed mills and livestock farms because of their simple structure, large loading capacity, material adaptability, and low maintenance requirements (Groen et al., 2015; Gu et al., 2006; Vertomrnen & Kinget, 1997; Zhao et al., 2019). Their design, however, still relies heavily on empirical scaling, and the matching of structural and operating parameters remains insufficient. Frequent problems include segregation of vitamins, minerals, and pharmaceutical additives, material retention near the chamber bottom, and high energy consumption per unit of product. The discrete element method (DEM) can resolve particle-scale motion and macroscopic mixing behavior and has therefore become an established tool for investigating powder and granular mixing equipment. Basinskas and Sakai (2016) used DEM with a signed-distance-function wall-boundary model to analyze axial diffusion in a single-screw mixer and to quantify the contributions of convection and diffusion to mixing efficiency. Halidan et al. (2016) examined the effect of interparticle cohesion on powder mixing in a ribbon mixer and provided a mechanistic interpretation of the observed mixing behavior. Jin et al.

(2022b) compared three impeller configurations in an industrial-scale U-shaped ribbon mixer and showed that the radial diffusion coefficient was highest and the axial diffusion coefficient was lowest; impeller configuration and loading pattern also interacted strongly. Tsugeno et al. (2021) related the swept volume of paddle motion to mixing performance and identified paddle width as an important structural parameter. Siraj et al. (2011) reported that paddle installation angle and particle size substantially affect the mixing of binary particle systems.

Most previous studies have focused on single-component granular materials or idealized binary mixtures, which limits their ability to describe the coupled convective, shear, and diffusive mixing of multicomponent TMR feeds under paddle agitation. The combined effects of paddle angle, rotor spacing, and rotational speed also remain insufficiently quantified, and systematic parameter optimization is still limited. To address these gaps, this study designs a twin-shaft paddle-type TMR mixer, investigates its particle-scale mixing behavior using DEM, and optimizes the paddle installation angle, rotor spacing, and main-shaft rotational speed with the Lacey mixing index as the response variable. A finite-element screening is also performed to assess the structural feasibility of the load-bearing assembly.

# 1. Overall structural design and operating principles

## 1.1. Overall structure

The proposed twin-shaft paddle-type TMR mixer consists of a double-arc mixing chamber, two parallel horizontal shafts, wedge-shaped paddle assemblies, a drive motor, a reducer, a synchronous gear pair, and feeding and discharge devices (Figure 1). Power is transmitted from the motor through the reducer and the gear pair to the two shafts, which rotate at the same speed in opposite directions. The paddles are arranged

in a discrete helical sequence along each shaft and are inclined to generate both axial transport and radial dispersion. The paddle-tip radius is matched to the inner chamber radius to maintain a small, uniform wall clearance. A discharge port fitted with a slide gate is located at the chamber bottom. This configuration is intended to provide high mixing efficiency and good adaptability to multicomponent, multiscale TMR feeds (Batel et al., 2026; Hidir et al., 2026; Lourenço, 2026).

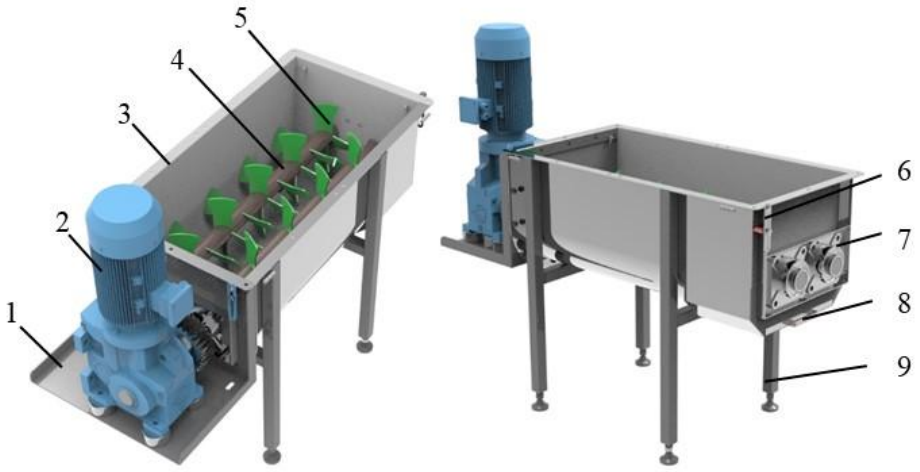


(a) Overall structure (b) Twin-shaft paddle assembly

1. Motor mounting base; 2. Motor; 3. Mixing chamber; 4. Drive shaft; 5. Paddle assembly; 6. Position sensor; 7. Bearings; 8. Discharge port; 9. Support frame

**Fig. 1.** Overall structure and rotor configuration of the twin-shaft paddle mixer.

### 1.2. Working principle

The mixer operates as a forced-convection bulk-material system. In the overlap region between the two counter-rotating shafts, the paddles lift material upward and outward, creating a localized fluidized zone in which particles are briefly suspended and then exchange between the two shaft regions. The inclined paddle faces simultaneously drive axial transport, while the end paddles redirect material between the two shafts and close the horizontal circulation loop. The resulting flow field is dominated by axial convection and supplemented by radial shear and particle-scale diffusion (Figure 2). Convective motion rapidly redistributes components at the macroscale, shear deformation disrupts agglomerates at the mesoscale, and diffusive

motion improves microscale homogeneity (Zhang et al., 2025b).

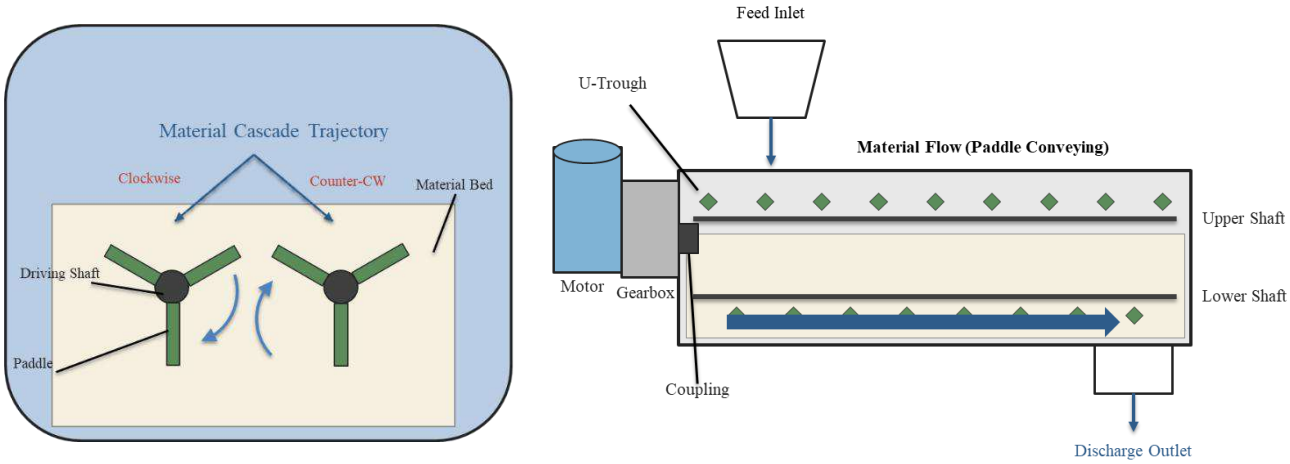


（a）Counter-rotating Convective Mixing (b) Material Flow and Discharge

**Fig. 2.** Working principle of the twin-shaft paddle mixer.

## 2. Design and analysis of key components

### 2.1. Design of the mixing chamber

The mixing chamber determines the available flow space, the distribution of shear, and the proportion of dead zones. The proposed chamber has an intersecting double-arc, double-Ω cross-section that follows the swept paths of the two rotors, thereby limiting stagnation zones while allowing unrestricted cross-shaft material exchange. The cross-section consists of two equal circular arcs connected at the center without an intermediate partition wall, forming an interconnected ∞-shaped working volume (Figure 3).

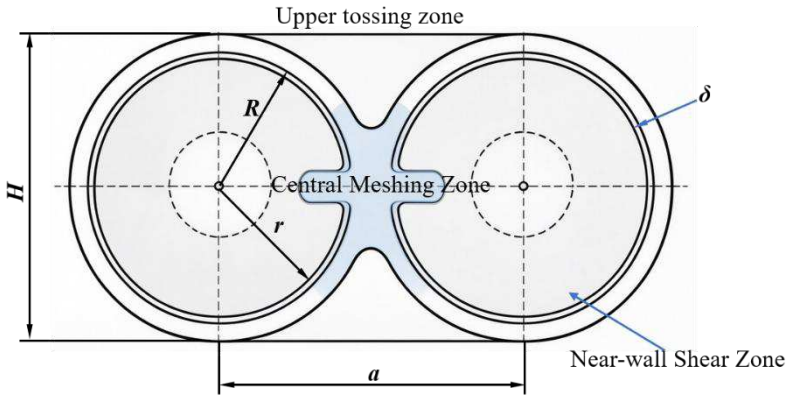

R, inner arc radius; a, rotor center distance; r, paddle-tip radius; δ, radial clearance; H, chamber height.

**Fig. 3.** Mixing chamber geometry and principal dimensions.

The chamber walls are formed from smooth, wear-resistant steel plates bent into two tangent circular-arc channels. The arc geometry is matched to the rotor trajectories to maintain a uniform clearance at the paddle tips and reduce material accumulation at the corners. To ensure effective mixing, the chamber design must satisfy the following geometric conditions:

$$\begin{cases} R = r + \delta \\ R < a < 2R \\ H = 2R + h_0 \end{cases} \quad (1)$$

The radial clearance δ between the paddle tips and the chamber wall was set to 5-15 mm, with 10-15 mm recommended for long-fiber TMR to reduce straw jamming and 5-10 mm for fine-particle feeds to enhance wall shear. The center-to-center rotor distance a was set to (1.6-1.8)R. A smaller distance narrows the central meshing zone and weakens cross-shaft convection, whereas an excessively large distance increases the central dead volume and reduces circulation efficiency. The height of the upper straight section, $h_0$, was set to (0.2-0.3)R to accommodate material expansion and prevent overflow. The chamber length-to-diameter ratio, L/D, was specified as 1.8-2.5; higher values can cause nonuniform axial mixing, whereas lower values shorten the residence time.

For a small-scale continuous-feed system, the chamber was dimensioned with an inner arc radius $R$ = 310 mm, a rotor center distance $a$ = 530 mm, a paddle-tip radius $r$ = 300 mm, a radial clearance $\delta$ = 10 mm, a total height $H$ = 1300 mm, and an effective working length $L$ = 1300 mm. The inner wall was fabricated from wear-resistant 304 stainless steel plate and polished to reduce feed adhesion. Thickened end plates integrate the bearing housings, and combined packing and air seals prevent leakage of fine particles.

The theoretical cross-sectional area of the chamber equals the combined area of the two intersecting circles minus their overlapping area. The working volume per unit length is therefore:

$$V = 2R\arccos(\frac{a}{2R}) - \frac{a}{2}\sqrt{4R^2 - a^2} \quad (2)$$

where $V$ is the chamber volume per unit length (mm²).

The effective working volume was determined from the recommended filling ratio for feed mixing, $\gamma$ = 0.4-0.6. A design value of $\gamma = 0.5$ was selected:

$$V_e = \gamma VL \quad (3)$$

where $V_e$ is the effective working volume (mm³).

Using Equations (2) and (3), the effective volume corresponds to a feed mass of approximately 152 kg at a bulk density of 400 kg/m³, which is consistent with the intended capacity of the small-scale household TMR system.

### 2.2. Design of the twin-rotor paddle assembly

The twin-rotor assembly is the core functional unit of the mixer. It comprises two parallel stepped shafts, multiple sets of wedge-shaped paddles, mounting brackets, and a synchronous drive mechanism (Figure 4). The shafts are horizontal and parallel, with their axes aligned along the chamber and their centers coinciding with the centers of the two chamber arcs. Equal-speed counter-rotation generates combined convective, shear, and diffusive mixing.

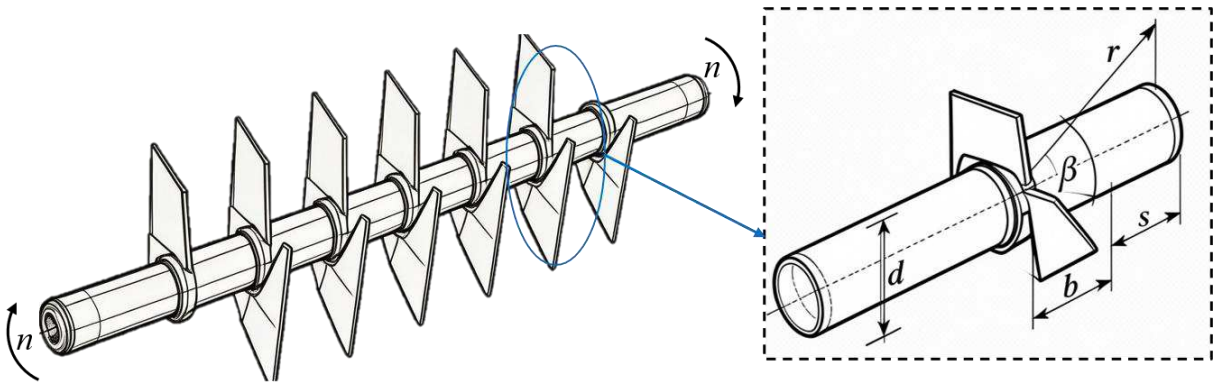


d, shaft diameter; r, paddle-tip radius; b, paddle width; s, axial distance between adjacent paddle sets; β, paddle installation angle.

**Fig. 4.** Twin-rotor paddle assembly and geometric parameters.

The paddles have a wedge-shaped, plow-like profile with an inclined working face that provides axial thrust and radial dispersion. Rounded cutting edges reduce material buildup and limit entanglement of fibrous straw during TMR mixing.

The principal paddle dimensions were determined as follows.

$$h = r - \frac{d}{2} \tag{4}$$

The paddle radial height is $h$ = 278 mm and the axial width is $b$ = 80 mm. Each paddle is bent from 5-mm-thick 304 stainless steel plate, and reinforcing ribs are welded to the rear face to increase stiffness. The cutting edge is ground to a rounded profile to reduce material adhesion and fiber entanglement.

Two paddles are mounted symmetrically at 180° in each cross-section to balance the rotational inertia. Adjacent paddle pairs are circumferentially offset by 90°, forming a discrete helical conveying sequence along the shaft. A 50 mm clearance is maintained at each end, giving an effective installation length of 1200 mm.

### 2.3. Analysis of material mixing dynamics

Feed mixing is a complex kinetic process in which multicomponent particles undergo spatial rearrangement, interfacial penetration, and agglomerate breakup under an external force field. The governing mechanisms are convective mixing, shear mixing, and diffusive mixing. In the proposed twin-shaft counter-rotating configuration, the interleaved paddles create a multidimensional, strongly coupled, and spatially zoned particle flow. These mechanisms act simultaneously, with different intensities among regions, and jointly determine the final mixing uniformity and efficiency.

Convective mixing is the dominant macroscopic mechanism in twin-shaft paddle mixers. It involves large-scale displacement of particle clusters and produces global redistribution of components through

circulating flow. Three coupled modes are present. First, radial ejection occurs when the rotating paddles lift material from the bottom and form a fluidized, low-contact-stress zone in the central overlap region (Figure 5a). Second, cross-shaft convection occurs as particles leave this zone, fall under gravity, and are exchanged between the two shaft regions. Third, axial circulation is generated by the helically arranged paddles and the end paddles, which redirect material between the shafts and close the horizontal circulation loop (Figure 5b). This combined motion increases the circulation frequency and broadens the spatial extent of mixing compared with a single-shaft paddle system. The alternating forces in the central overlap region also reduce the tendency toward stable stratification and density segregation.

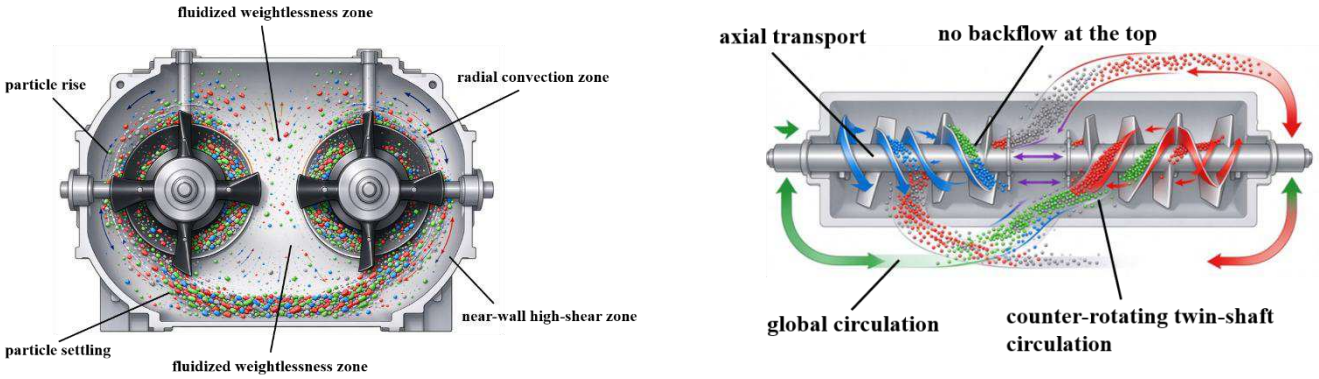


a. Cross-sectional radial motion

b. Axial macroscopic convection

**Fig. 5.** Convective mixing mechanisms: (a) radial motion and (b) axial circulation**.**

Shear mixing arises from relative slippage and velocity gradients between adjacent material layers. In the proposed mixer, shear is concentrated in three regions: the clearance between the paddle tips and the chamber wall, the intermeshing zone between the two rotors, and the distributed shear layer within the moving particle bed. High-speed paddles scour the wall and disperse fibrous clumps, while counter-directional motion in the meshing zone subjects agglomerates to alternating shear. These effects are particularly important for viscous feed and compacted straw. Distributed shear within the bed further promotes interlayer migration and component penetration.

Diffusive mixing redistributes individual particles through random motion, free-fall filling, and relative

sliding, and is therefore critical to final microscale uniformity (Figure 6). In the central fluidized zone, reduced interparticle constraint allows fine feed powder and mineral additives to penetrate voids within the coarse particle matrix. Shear-induced diffusion occurs when particles move stochastically along shear planes, while falling-fill diffusion occurs as lifted particle clusters disperse and occupy voids below. The multi-level shear and repeated vertical exchange in the twin-shaft system maintain these mechanisms over a range of operating speeds and improve final homogeneity.

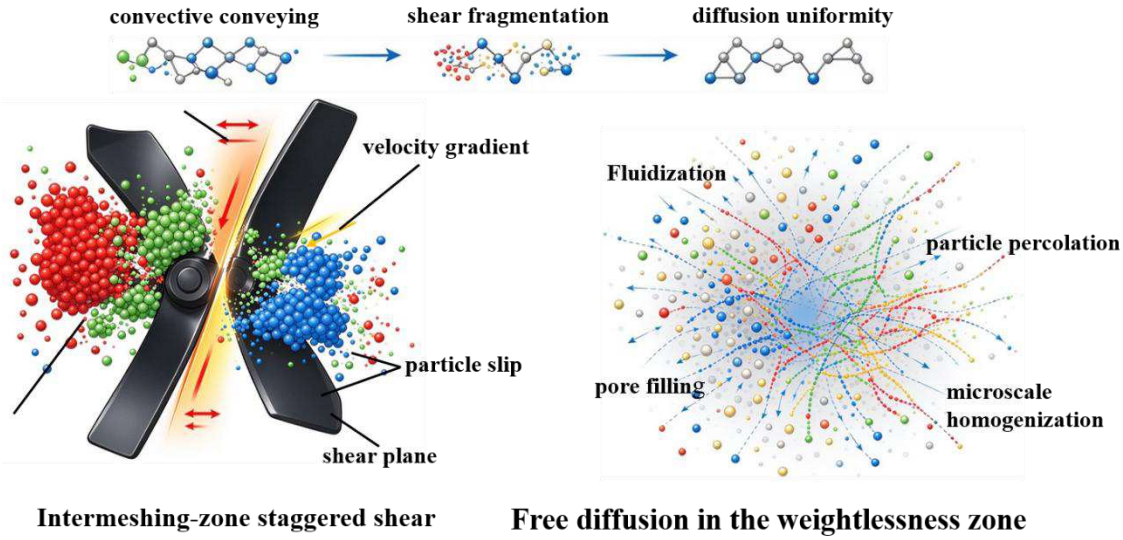


**Fig. 6.** Shear-induced diffusion and particle-scale mixing mechanisms.

The paddle installation angle β, defined as the angle between the inclined paddle face and the radial plane of the shaft, governs the partition between axial thrust and radial lift. Increasing β enhances axial transport and convective circulation but reduces radial dispersion and shear. The axial spacing between adjacent paddle sets, s, controls the continuity of axial transport and the extent of local dead zones. Excessively small spacing increases compression and power demand, whereas excessively large spacing reduces axial renewal. The main-shaft rotational speed n controls the paddle-tip velocity and is the most readily adjustable operating parameter. Higher speeds increase shear and ejection but can cause excessive fiber breakage, power consumption, and noise. These three parameters were therefore selected for the

subsequent optimization.

Because these geometric and operating parameters also determine the loads transmitted to the chamber and rotors, the structural feasibility of the load-bearing assembly was assessed before the DEM optimization.

### 2.4. Finite-element assessment of the load-bearing assembly

A linear elastic finite-element model of the mixing chamber and rotor assembly was developed in SolidWorks Simulation. The chamber was represented by a 3 mm Q235 steel shell, and the rotor shaft and paddles were assigned the same material grade. The material properties were $E = 210$ GPa, $\nu = 0.28$, $\rho = 7800$ kg·m$^{-3}$, and yield strength $\sigma_y = 220.59$ MPa. The analysis served as a design-stage strength and modal screening; plasticity, weld details, bolt preload, particle contact loads, and transient forcing were not included.

The design torque was estimated from the rated drive power and shaft speed (Figure 8A). For $P = 3$ kW and $n = 24.85$ r/min, the theoretical shaft torque was $T_0 = 9550P/n = 1153$ N·m. Applying a transmission efficiency $\eta = 0.93$ and a working shock factor $K = 1.30$ gave a design torque of approximately 1.40 kN·m. The equivalent stress distributions of the chamber and rotor shaft are shown in Figure 7A and Figure 7B, respectively. The maximum shaft stress was 207.98 MPa at the keyway fillet. Figure 8B compares this peak with the tabulated yield strength; the stress remained 12.61 MPa below yield, corresponding to 94.3% utilization. The chamber stress remained below the allowable limit according to the source analysis, but its maximum value was not reported and was therefore not used for quantitative comparison. Because the shaft peak is located at a geometric stress raiser, mesh convergence and a local submodel are required before interpreting the value as a structural limit.

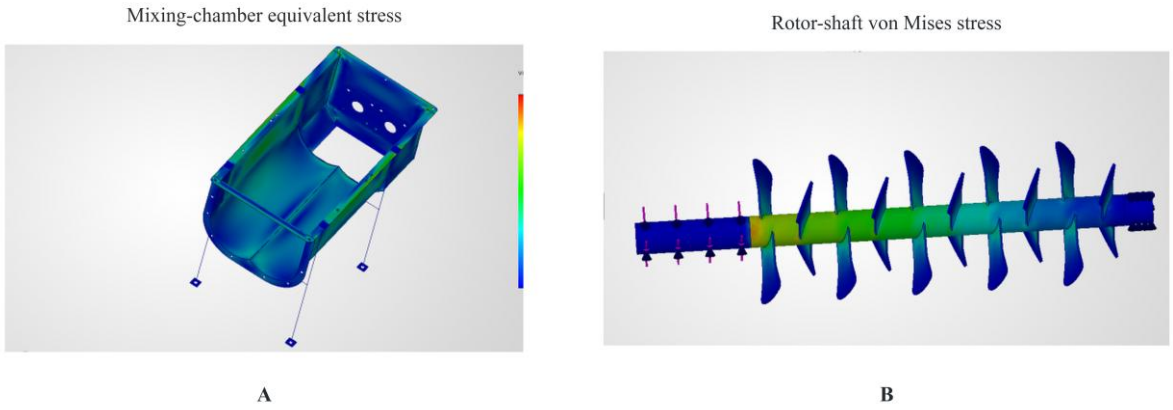


**Fig. 7.** Equivalent stress distributions of the load-bearing assembly.

A, Qualitative equivalent stress field in the mixing chamber under the rated load; the maximum remained below the allowable limit, but no numerical value was reported. B, von Mises stress field in the rotor shaft under the design torque; the reported peak is 207.98 MPa at the keyway fillet. Quantitative checks are shown in Fig. 8.

Free-vibration analysis produced chamber natural frequencies of 23.963-98.085 Hz, with the first mode dominated by lateral sway of the frame. The shaft analysis returned a 0 Hz rigid-body rotation mode, a first bending pair at 73.12 and 73.15 Hz, a second pair at 247.85 and 248.26 Hz, and a paddle-dominated mode at 258.83 Hz. At the rated shaft speed, the rotational frequency was 0.414 Hz. The first elastic chamber and shaft modes were therefore 57.9 and 176.6 times the rated frequency, respectively (Figure 8C,D). This separation makes direct first-order excitation of these global flexible modes unlikely.

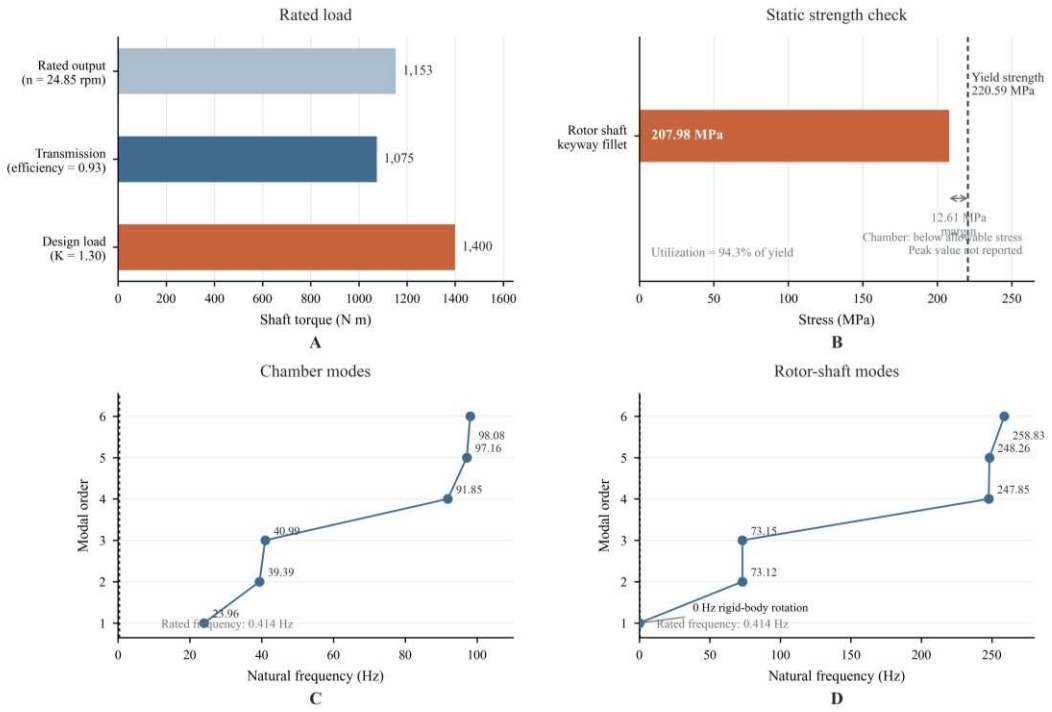


**Fig. 8.** Quantitative structural verification of the rated twin-shaft mixer.

A, Design torque chain; B, peak shaft stress relative to the tabulated Q235 yield strength; C, chamber natural frequencies; D, rotor-shaft natural frequencies, including the 0 Hz rigid-body mode. The rated shaft frequency (0.414 Hz) is indicated in C and D.

Taken together, the static and modal results support the structural feasibility of the load-bearing assembly at the rated design point. The shaft remained below yield under the 1.30 shock factor, and the flexible modes were well separated from the rated rotational frequency. However, the limited local stress margin and the simplified representation of bearings, welds, and excitation sources restrict this analysis to a preliminary structural screen. Realistic bearing stiffness, a converged keyway submodel, and excitation spectra for the transmission and paddle-passing frequencies are required before forced-response safety can be established.

These finite-element results define the structural operating envelope of the load-bearing assembly. The particle-scale flow and mixing performance within the same chamber geometry were then investigated using a discrete-element model, as described in Section 3.

## 3. Discrete element simulation of the twin-shaft paddle mixer

Orthogonal DEM simulations were performed in EDEM to quantify the effects of paddle installation angle, rotor spacing, and main-shaft rotational speed on mixing uniformity. The relative importance of the factors and their optimal combination were determined to support the structural design and operational control of small-scale domestic TMR mixers.

### 3.1. Simulation model and parameter settings

A simplified geometric model was created in SolidWorks using the design parameters. Bearing housings and seals were omitted because they do not materially affect the particle flow. The model retained the mixing chamber, two main shafts, and wedge-shaped paddles and was exported in STEP format for import into EDEM (Figure 9). Each shaft was defined as a rotating body, and the two shafts were assigned equal speeds in opposite directions. Particles were generated in the upper feed zone using the Particle Factory function, with sizes following a normal distribution to represent the variability of real TMR feed.

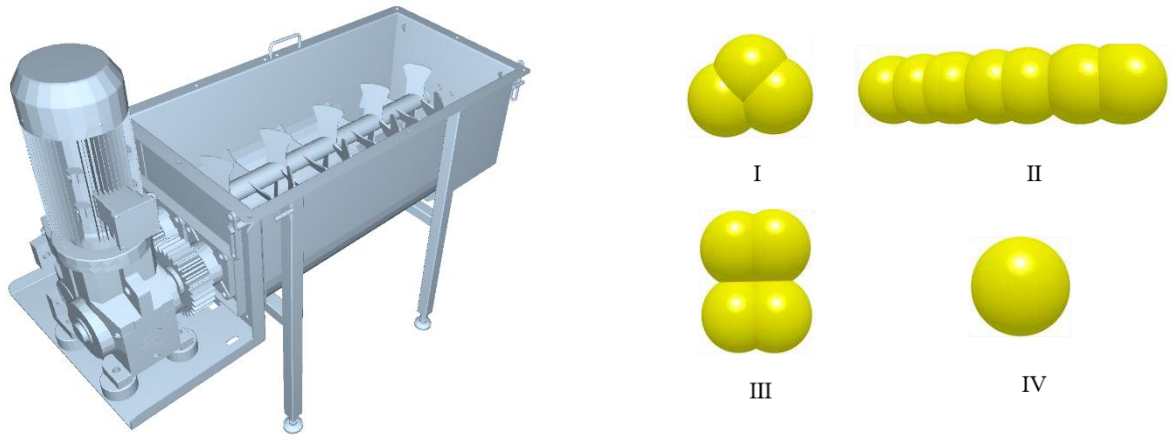


a. Mixer assembly b. Feed particles

**Fig. 9.** Discrete-element model: (a) mixer assembly and (b) feed particles.

Matrix and tracer particles were generated at a 9:1 mass ratio. All particle groups had the same density

and contact coefficients and were distinguished only by their IDs, thereby avoiding segregation caused by differing physical properties. Particles were allowed to settle for approximately 100 s before shaft rotation began. The four particle groups contained 40,000, 30,000, 35,000, and 40,000 particles, respectively, for a total of 145,000. The Hertz-Mindlin contact model was used to resolve particle contacts and dynamic flow (Haque et al., 2021; Kong et al., 2022; Liu et al., 2027; Tang et al., 2024; Zeng et al., 2021; Zhang et al., 2025a; Zhang et al., 2025b). A fixed time step of $2 \times 10^{-6}$ s, corresponding to 10-20% of the critical Rayleigh time, was selected to balance accuracy and computational cost. Contact parameters were adopted from previous calibration studies (Ghafori & Ataei, 2026; Ghodki et al., 2026; Kong et al., 2024; Li et al., 2025). The simulation parameters are summarized in Table 1, and representative mixing states are shown in Figure 10.

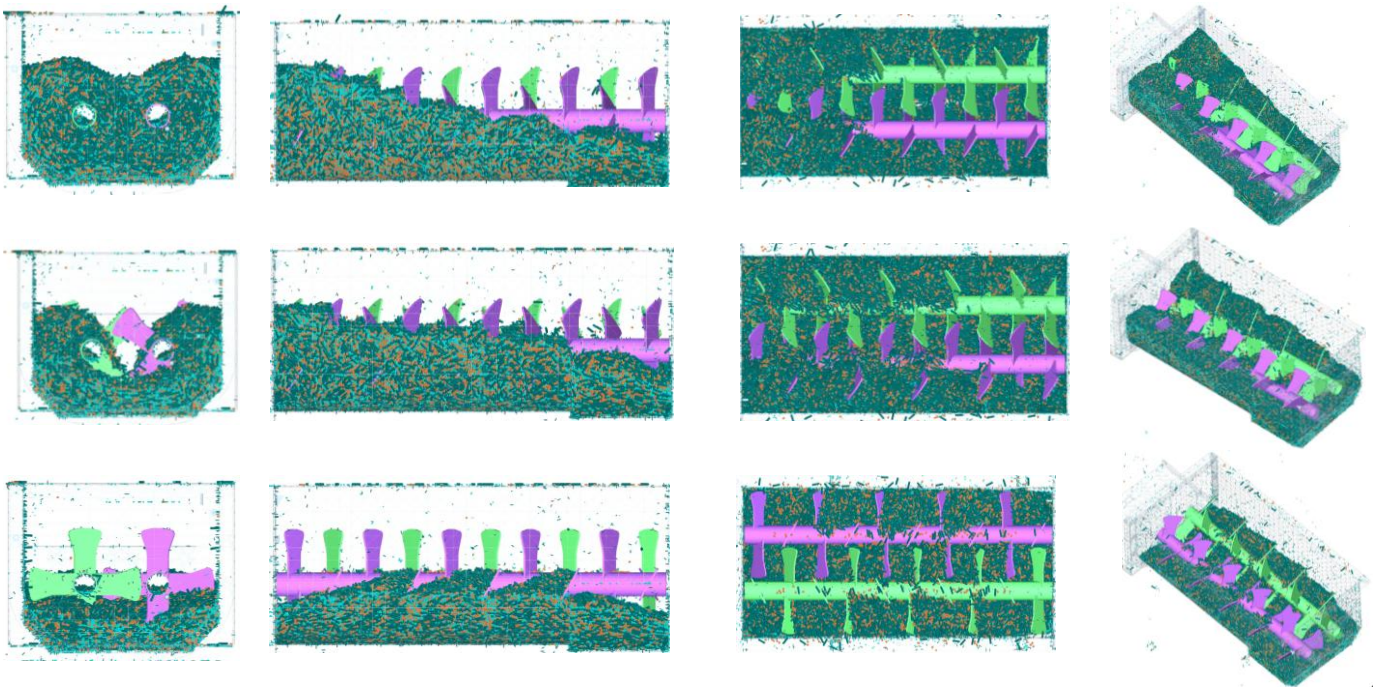

**Fig. 10.** Mixing states of the twin-shaft paddle mixer under the side-by-side initial loading condition.

### 3.2. Mixing performance evaluation

The Lacey mixing index M was used to evaluate mixing performance under different structural and

operating conditions (Jin et al., 2022a). M ranges from complete segregation to complete random mixing. A threshold of M = 0.90 was adopted as the acceptance criterion, and T denotes the time required to reach this threshold. The Lacey index was calculated as:

$$M = \frac{\sigma_0^2 - \sigma^2}{\sigma_0^2 - \sigma_\tau^2}$$

where $\sigma_0^2$ is the variance of the component fraction in the completely segregated initial state, $\sigma^2$ is the measured variance of the tracer-particle volume fraction at a given time, and $\sigma_r^2$ is the theoretical variance for complete random mixing.

**Table 1.** Material and contact parameters used in the DEM simulations.

| Material | Parameter | Value |
|---|---|---|
| Raw feed | Density (kg·m⁻³) | 810 |
| | Poisson's ratio | 0.40 |
| | Shear modulus (MPa) | $1.14 \times 10^6$ |
| Stainless steel | Density (kg·m⁻³) | $7.87 \times 10^3$ |
| | Poisson's ratio | 0.39 |
| | Shear modulus (MPa) | $8.9 \times 10^2$ |
| Particle I | Coefficient of restitution (steel, I, II, III, IV) | 0.37, 0.31, 0.29, 0.35, 0.35 |
| | Coefficient of static friction (steel, I, II, III, IV) | 0.65, 0.32, 0.40, 0.60, 0.20, 0.30 |
| | Coefficient of kinetic friction (steel, I, II, III, IV) | 0.17, 0.12, 0.10, 0.09, 0.12 |
| Particle II | Coefficient of restitution (steel, II, III, IV) | 0.37, 0.31, 0.21, 0.35 |
| | Coefficient of static friction (steel, II, III, IV) | 0.65, 0.35, 0.32, 0.31 |
| | Coefficient of kinetic friction (steel, II, III, IV) | 0.17, 0.12, 0.09, 0.10 |
| Particle III | Coefficient of restitution (steel, III, IV) | 0.31, 0.25, 0.30 |
| | Coefficient of static friction (steel, III, IV) | 0.45, 0.29, 0.32 |
| | Coefficient of kinetic friction (steel, III, IV) | 0.12, 0.12, 0.20 |
| Particle IV | Coefficient of restitution (steel, IV) | 0.17, 0.23 |
| | Coefficient of static friction (steel, IV) | 0.34, 0.36 |
| | Coefficient of kinetic friction (steel, IV) | 0.09, 0.10 |

### 3.3. Orthogonal simulation and parameter optimization

#### 3.3.1. Experimental design

The preceding mixing analysis identified the paddle installation angle, rotor spacing, and main-shaft rotational speed as the principal factors affecting uniformity. The experimental ranges were 19.8-70.2°, 315.9-484.1 mm, and 26.4-93.6 r/min, respectively. The coded factor levels are listed in Table 2. Using the steady-state Lacey index M as the response, a response-surface design was generated in Design-Expert 8.0.6 and evaluated using DEM. The experimental scheme and results are summarized in Table 3.

**Table 2.** Coded levels and actual values of the experimental factors.

| Level | Paddle installation angle, $x_1$ (degrees) | Rotor spacing, $x_2$ (mm) | Shaft speed, $x_3$ (r/min) |
|---|---|---|---|
| -1.682 | 19.8 | 315.9 | 26.4 |
| -1 | 30.0 | 350.0 | 40.0 |
| 0 | 45.0 | 400.0 | 60.0 |
| 1 | 60.0 | 450.0 | 80.0 |
| 1.682 | 70.2 | 484.1 | 93.6 |

**Table 3.** Response-surface design and simulation results.

| Test Number | Factors | | | Performance specification |
|---|---|---|---|---|
| | $x_1$ | $x_2$ | $x_3$ | Lacey index, M |
| 1 | -1.0 | -1.0 | -1.0 | 0.8810 |
| 2 | -1.0 | -1.0 | +1.0 | 0.8724 |
| 3 | -1.0 | +1.0 | -1.0 | 0.8696 |
| 4 | -1.0 | +1.0 | +1.0 | 0.8671 |
| 5 | +1.0 | -1.0 | -1.0 | 0.8601 |
| 6 | +1.0 | -1.0 | +1.0 | 0.8661 |
| 7 | +1.0 | +1.0 | -1.0 | 0.8793 |
| 8 | +1.0 | +1.0 | +1.0 | 0.8821 |
| 9 | +1.682 | 0 | 0 | 0.8715 |

| Test Number | Factors | | | Performance specification |
|---|---|---|---|---|
| | $x_1$ | $x_2$ | $x_3$ | Lacey index, M |
| 10 | -1.682 | 0 | 0 | 0.8756 |
| 11 | 0 | +1.682 | 0 | 0.8857 |
| 12 | 0 | -1.682 | 0 | 0.8857 |
| 13 | 0 | 0 | +1.682 | 0.8602 |
| 14 | 0 | 0 | -1.682 | 0.8516 |
| 15 | 0 | 0 | 0 | 0.9231 |
| 16 | 0 | 0 | 0 | 0.9278 |
| 17 | 0 | 0 | 0 | 0.9259 |

### 3.3.2. Analysis of variance and factor effects

The analysis of variance is summarized in Table 4. The quadratic regression model was highly significant ($F = 104.86$, $P < 0.0001$) and achieved $R^2 = 0.9895$ and adjusted $R^2 = 0.9801$. The lack-of-fit test was not significant ($F = 2.55$, $P = 0.164$), indicating that the model adequately represented the simulated response. The linear terms $x_1$, $x_2$, and $x_3$ were not significant within the experimental range, indicating the absence of a simple linear effect. The $x_1 \times x_2$ interaction was highly significant ($F = 23.11$, $P = 0.0007$), whereas $x_1 \times x_3$ and $x_2 \times x_3$ were not significant. The negative coefficients of the significant quadratic terms indicate concave responses with interior optima. On the basis of the quadratic-term F values, mixing uniformity was most sensitive to main-shaft speed ($F = 576.89$), followed by paddle installation angle ($F = 317.27$) and rotor spacing ($F = 183.32$).

**Table 4.** Analysis of variance for the quadratic response-surface model.

| Source | Statistics | | | |
|---|---|---|---|---|
| | Sum of squares | df | F | P |
| Model | 0.0137 | 9 | 104.9 | <0.0001** |
| $x_1$ | $6.46 \times 10^{-6}$ | 1 | 0.4 | 0.52 |
| $x_2$ | $2.5 \times 10^{-5}$ | 1 | 1.7 | 0.219 |

| Source | Statistics | | | |
|---|---|---|---|---|
| | Sum of squares | df | F | P |
| $x_3$ | $1.1 \times 10^{-5}$ | 1 | 0.7 | 0.4084 |
| $x_1 \times x_2$ | $3.7 \times 10^{-4}$ | 1 | 23.1 | 0.0007** |
| $x_1 \times x_3$ | $5.0 \times 10^{-5}$ | 1 | 3.4 | 0.0951 |
| $x_2 \times x_3$ | $1.0 \times 10^{-6}$ | 1 | 0.1 | 0.7937 |
| $x_1^2$ | $4.6 \times 10^{-3}$ | 1 | 317.3 | <0.0001** |
| $x_2^2$ | $2.6 \times 10^{-3}$ | 1 | 183.3 | <0.0001** |
| $x_3^2$ | $8.4 \times 10^{-3}$ | 1 | 576.9 | <0.0001** |
| Residuals | $1.5 \times 10^{-4}$ | 10 | | |
| Lack of fit | $1.2 \times 10^{-4}$ | 5 | 2.55 | 0.1639 |
| Pure error | $2.4 \times 10^{-5}$ | 5 | | |
| Total | $1.4 \times 10^{-2}$ | 19 | | |

### 3.3.3. Response-surface analysis

The response surfaces in Figure 11 show the pairwise effects of the factors on M when the third factor was held at its central level. In Figure 11a, with the shaft speed fixed at 60 r/min, M reached a maximum of approximately 0.92 near the central paddle angle and rotor spacing and decreased to approximately 0.86 toward the corners. The slightly elliptical contours indicate a significant interaction between paddle angle and rotor spacing. Figure 11b shows a steeper response gradient along the speed axis than along the paddle-angle axis: deviations from 60 r/min reduced M more rapidly, whereas M changed gradually over 30-60°. Figure 11c shows the weakest interaction, with the response varying only moderately with rotor spacing in the range of 350-450 mm. The model therefore predicted an optimum near 45°, 400 mm, and 60 r/min, with $M \approx 0.92$, consistent with the central-point replication results.

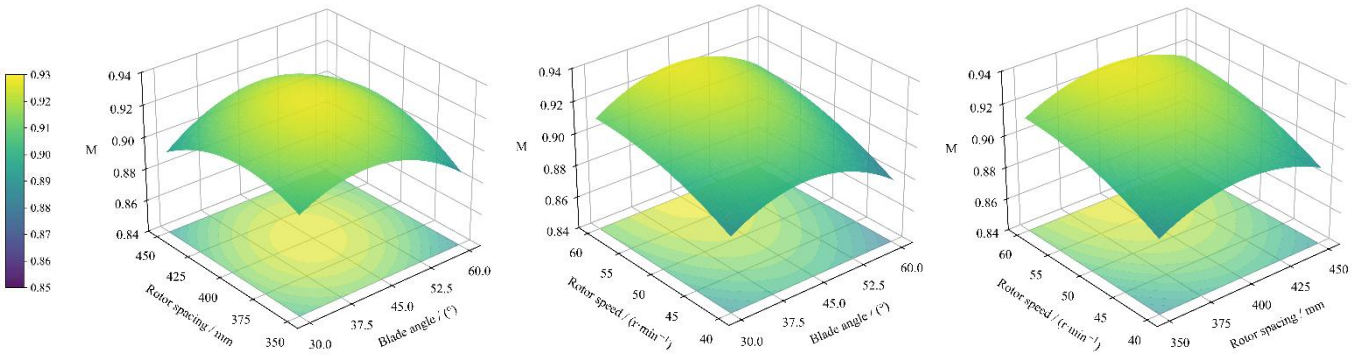


**Fig. 11.** Response surfaces of the Lacey mixing index M

(a) paddle angle and rotor spacing at 60 r/min; (b) paddle angle and shaft speed at 400 mm; and (c) rotor spacing and shaft speed at 45°.

### 3.3.4. Parameter optimization and numerical verification

Constrained maximization of M was performed using Design-Expert 8.0.6 over the full experimental ranges: paddle angle 20-70°, rotor spacing 316-484 mm, and shaft speed 26-94 r/min. The numerical optimum was 44.7°, 402.5 mm, and 60.4 r/min, with a predicted M of 0.9263. Considering manufacturing tolerances and practical adjustment, the design values were rounded to 45°, 400 mm, and 60 r/min. A verification simulation at this configuration produced M = 0.91, satisfying the acceptance threshold of 0.90.

## 3.4. Limitations and scope of interpretation

Several constraints define the scope of the present analysis. The DEM contact parameters were adopted from previous calibration studies rather than calibrated against measurements for the specific TMR mixture, and the optimized configuration was assessed through a verification simulation rather than physical mixing trials. Consequently, the Lacey index characterizes simulated mixing under the specified particle model and loading conditions and does not by itself establish mixing time, energy consumption, material residue, or long-term operational performance. The finite-element assessment was a linear elastic design-stage screen that omitted plasticity, weld details, bolt preload, particle contact loads, and transient forcing. It therefore supports preliminary structural feasibility rather than a forced-response safety assessment. Physical mixing tests, energy and residue measurements, and a refined structural model with bearing stiffness and a

converged keyway submodel are required to evaluate these outcomes.

## 4. Conclusions

A twin-shaft paddle-type TMR mixer was designed with axial convection as the primary mixing mechanism and radial shear as a supplementary mechanism. DEM simulations and response-surface optimization were used to characterize the mixing behavior and identify an appropriate design configuration. The main conclusions are as follows.

(1) The counter-rotating shafts created a fluidized zone in the central overlap region and a strong shear layer near the paddle tips, producing a composite circulation pattern of axial transport along the paddle flights and central cross-shaft recirculation. This flow pattern is expected to improve the dispersion of trace components in multicomponent TMR feeds.

(2) A three-factor quadratic model based on the Lacey index was highly significant ($F = 104.86$, $R^2 = 0.9895$) and showed no significant lack of fit ($F = 2.55$, $P = 0.164$). Within the studied factor ranges, the model therefore provided a suitable basis for response prediction and constrained optimization.

(3) The factors affecting mixing uniformity decreased in importance in the order of main-shaft speed, paddle installation angle, and rotor spacing. The significant angle-spacing interaction indicates that these two geometric parameters should be designed jointly rather than optimized independently.

(4) Constrained optimization produced an optimum of 44.7°, 402.5 mm, and 60.4 r/min, with a predicted M of 0.9263. The practical configuration of 45°, 400 mm, and 60 r/min achieved a simulated M of 0.91. A design-stage finite-element screening further showed that the shaft remained below the tabulated yield strength under the rated load, while the critical flexible modes remained well above the rated rotational frequency.

Within these stated boundaries, the simulation results provide a preliminary basis for the structural and operating-parameter design of twin-shaft paddle TMR mixers.

## Author contributions

Wei Song: Conceptualization, Methodology, Software, Formal analysis, Investigation, Data curation, Visualization, Validation, Writing - original draft, Writing - review and editing. Bin Luo and Yongkun Zhang: Investigation, Methodology, Validation, Writing - review and editing. Liu Hongyun: Conceptualization, Methodology, Formal analysis, Validation, Supervision, Funding acquisition, Writing - review and editing.

## Funding

This work was supported by the Jiangxi Provincial Key Laboratory of Modern Agricultural Equipment (Grant No. 20242BCC32127).

## Declaration of competing interest

The authors declare that they have no known competing financial interests or personal relationships that could have appeared to influence the work reported in this paper.

## Data availability

No or not applicable. This manuscript does not report data generation or analysis.

## References

Basinskas, G., & Sakai, M. (2016). Numerical study of the mixing efficiency of a ribbon mixer using the discrete element method. Powder Technology, 287, 380–394. https://doi.org/10.1016/j.powtec.2015.10.017.

Batel, M.-A., Contardo, L., Gatumel, C., & Berthiaux, H. (2026). Intensification of a continuous powder mixing process by distributed and/or delayed feeding. Powder Technology, 473, 122229. https://doi.org/10.1016/j.powtec.2026.122229.

Bergeron, A. N., Stark, C., Boney, J. W., Goldsmith, T., Pope, J. T., Bradshaw, S., & Shirely, R. B. (2026). The feed milling process: A focus on the pelleting, liquid application, and their effects on animal production. Journal of Applied Poultry Research, 35(3), 100705. https://doi.org/10.1016/j.japr.2026.100705.

Ghafori, H., & Ataei, S. (2026). Hybrid CFD-DEM and ANN modeling of pneumatic conveying of aquaculture feed pellets: Flow regimes, mechanical damage, and performance optimization. Journal of Agriculture and Food Research, 31, 103285. https://doi.org/10.1016/j.jafr.2026.103285.

Ghodki, B. M., Sharma, A., & Chhetri, K. B. (2026). Advancements in CFD-DEM coupling for modeling and optimizing food granulation processes. Chemical Engineering Research and Design, 226, 450–464. https://doi.org/10.1016/j.cherd.2026.01.019.

Groen, M. J., Steele, M. A., & DeVries, T. J. (2015). Short communication: Effect of straw inclusion rate in a dry total mixed ration on the behavior of weaned dairy calves. Journal of Dairy Science, 98(4), 2693–2700. https://doi.org/10.3168/jds.2014-8978.

Gu, L., Liew, C. V., Soh, J. L. P., & Heng, P. W. S. (2006). Feasibility of eliminating premixing for the production of pellets in a rotary processor. Pharmaceutical Development and Technology, 11(2), 159–165. https://doi.org/10.1080/10837450600561240.

Halidan, M., Chandratilleke, G. R., Dong, K. J., & Yu, A. (2016). The effect of interparticle cohesion on powder mixing in a ribbon mixer. AIChE Journal, 62(4), 1023–1037. https://doi.org/10.1002/aic.15101.

Haque, A., Salama, A., Lo, K., & Wu, P. (2021). Surface and groundwater interactions: A review of coupling strategies in detailed domain models. Hydrology, 8(1), 35. https://doi.org/10.3390/hydrology8010035.

Hidir, A., Aaqillah-Amr, M. A., Abdul Rahim, K. A., Azra, M. N., Ma, H., Shapawi, R., Mat Noordin, N., & Ikhwanuddin, M. (2026). Sustainable feed processing methods to enhance growth and digestibility in freshwater aquaculture: A review. Animal Nutrition, 25, 228–245. https://doi.org/10.1016/j.aninu.2025.07.011.

Jin, X., Chandratilleke, G. R., Wang, S., & Shen, Y. (2022a). DEM investigation of mixing indices in a ribbon mixer. Particuology, 60, 37–47. https://doi.org/10.1016/j.partic.2021.03.005.

Jin, X., Wang, S., & Shen, Y. (2022b). DEM study of the effect of impeller design on mixing performance in a U-shape ribbon mixer. Advanced Powder Technology, 33(1), 103334. https://doi.org/10.1016/j.apt.2021.10.026.

Kong, X., Liu, J., Yang, T., Su, Y., Geng, J., & Niu, Z. (2022). Numerical simulation of feed pellet breakage in pneumatic conveying. Biosystems Engineering, 218, 31–42. https://doi.org/10.1016/j.biosystemseng.2022.03.012.

Kong, X., Cao, Q., & Niu, Z. (2024). Experimental research on breakage characteristics of feed pellets under different loading methods. Agriculture, 14(8), 1401. https://doi.org/10.3390/agriculture14081401.

Li, H., Kong, X., Jiang, S., & Niu, Z. (2025). DEM study on crushing and screening performance of maize kernel in hammer mill. Computational Particle Mechanics, 12(5), 3449–3459. https://doi.org/10.1007/s40571-025-01024-w.

Liu, X., Zhang, Z., & Liu, M. (2027). Overcoming scale disparity: A cross-scale CFD-DEM framework for modeling particulate flows with arbitrary size ratios. Journal of Computational Physics, 568, 115349. https://doi.org/10.1016/j.jcp.2026.115349.

Lourenço, M. (2026). Review: Trends in feed technology and feed additives for a sustainable and resilient livestock production. Animal, 101909. https://doi.org/10.1016/j.animal.2026.101909.

Lyu, F., Thomas, M., Hendriks, W. H., & van der Poel, A. F. B. (2020). Size reduction in feed technology and methods for determining, expressing and predicting particle size: A review. Animal Feed Science and Technology, 261, 114347.

https://doi.org/10.1016/j.anifeedsci.2019.114347.

Niu, Z., Kong, X., Shen, B., Li, H., Geng, J., & Liu, J. (2022). Parameters calibration of discrete element simulation for pellet feed attrition. Transactions of the Chinese Society for Agricultural Machinery, 53(7), 132–140, 207. https://doi.org/10.6041/j.issn.1000-1298.2022.07.013.

Schären, M., Jostmeier, S., Ruesink, S., Hüther, L., Frahm, J., Bulang, M., Meyer, U., Rehage, J., Isselstein, J., Breves, G., & Dänicke, S. (2016). The effects of a ration change from a total mixed ration to pasture on health and production of dairy cows. Journal of Dairy Science, 99(2), 1183–1200. https://doi.org/10.3168/jds.2015-9873.

Siraj, M. S., Radl, S., Glasser, B. J., & Khinast, J. G. (2011). Effect of blade angle and particle size on powder mixing performance in a rectangular box. Powder Technology, 211(1), 100–113. https://doi.org/10.1016/j.powtec.2011.04.004.

Sova, A. D., LeBlanc, S. J., McBride, B. W., & DeVries, T. J. (2014). Accuracy and precision of total mixed rations fed on commercial dairy farms. Journal of Dairy Science, 97(1), 562–571. https://doi.org/10.3168/jds.2013-6951.

Tang, H., Zhu, G., Xu, W., Xu, C., & Wang, J. (2024). Discrete element method simulation of rice grains impact fracture characteristics. Biosystems Engineering, 237, 50–70. https://doi.org/10.1016/j.biosystemseng.2023.11.011.

Tian, F., Chen, Y., Song, Z., Yan, Y., Li, F., & Wang, Z. (2020). Design and experiment of self-propelled TMR preparation mixer for silage straw feed. Transactions of the Chinese Society for Agricultural Machinery, 51(3), 106–114. https://doi.org/10.6041/j.issn.1000-1298.2020.03.012.

Tsugeno, Y., Sakai, M., Yamazaki, S., & Nishinomiya, T. (2021). DEM simulation for optimal design of powder mixing in a ribbon mixer. Advanced Powder Technology, 32(5), 1735–1749. https://doi.org/10.1016/j.apt.2021.03.026.

Vertomrnen, J., & Kinget, R. (1997). The influence of five selected processing and formulation variables on the particle size, particle size distribution, and friability of pellets produced in a rotary processor. Drug Development and Industrial Pharmacy, 23(1), 39–46. https://doi.org/10.3109/03639049709148480.

Wanapat, M., Suriyapha, C., Dagaew, G., Prachumchai, R., Phupaboon, S., Sommai, S., & Matra, M. (2024). The recycling of tropical fruit peel waste-products applied in feed additive for ruminants: Food manufacturing industries, phytonutrient properties, mechanisms, and future applications. Journal of Agriculture and Food Research, 17, 101234. https://doi.org/10.1016/j.jafr.2024.101234.

Zeng, Z., Ma, X., Cao, X., Li, Z., & Wang, X. (2021). Critical review of applications of discrete element method in agricultural engineering. Transactions of the Chinese Society for Agricultural Machinery, 52(4), 1–20. https://doi.org/10.6041/j.issn.1000-1298.2021.04.001.

Zhang, Q., Zheng, Z., Liao, Q., Yu, L., Liao, Y., & Wan, X. (2025a). Application status and prospect of coupled simulation in agricultural engineering research. Transactions of the Chinese Society for Agricultural Machinery, 56(7), 20–37, 149. https://doi.org/10.6041/j.issn.1000-1298.2025.07.002.

Zhang, W., Jiang, S., Kong, X., Geng, J., Niu, Z., & Li, H. (2025b). Analysis of impact characteristics of hammermill screen based on discrete element method and calibration of contact parameters of crushed particles. Transactions of the Chinese Society for Agricultural Machinery, 56(4), 501–511. https://doi.org/10.6041/j.issn.1000-1298.2025.04.047.

Zhao, S., Ding, W., Zhao, S., Gu, J., & Zhang, J. (2019). Performance analysis and optimization of pneumatic fishpond feeder based on EDEM-Fluent coupling. Transactions of the Chinese Society for Agricultural Machinery, 50(9), 130–139. https://doi.org/10.6041/j.issn.1000-1298.2019.09.015.